Nanoscale Research Letters

NANO EXPRESS   **Open Access**

Preparation and Magnetic Properties of Cobalt-Doped FeMn$_2$O$_4$ Spinel Nanoparticles

Aleksandr A. Spivakov, Chun-Rong Lin* , En-Szu Lin, Ying-Zhen Chen and Yaw-Teng Tseng

Abstract

Mixed-metal oxide nanoparticles have attracted great scientific interest since they find applications in many fields. However, the synthesis of size-controlled and composition-tuned mixed-metal oxide nanoparticles is a great challenge that complicates their study for practical application. In this study, Co-doped FeMn$_2$O$_4$ nanoparticles were synthesized by the solvothermal method in which the crystallization was carried out under autogenous pressure at temperatures of 190 °C for 24 h. The influence of Co doping on the evolution of the structural and magnetic properties was investigated by various methods. It was found from XRD data that crystallite size decreases from 9.1 to 4.4 nm with the increase in Co content, which is in good agreement with the results of TEM. Based on the results of magnetic measurements, it was found that the saturation magnetization first increases with an increase in the cobalt content and reaches its maximum value at $x = 0.4$, and a further increase in x leads to a decrease in the saturation magnetization. The influence of cation redistribution on the observed changes has been discussed.

Keywords: FeMn$_2$O$_4$ nanoparticles, Spinel ferrite, Cobalt doping, Magnetic properties

Introduction

Due to the unique magnetic, electrical, and other properties, spinel oxides have attracted great scientific interest and find practical applications in various fields, such as spintronic devices, data storage, supercapacitors, biomedicine, light absorption, environmental remediation, and so on [1–7]. One of the reasons for the wide variety of physicochemical properties of spinel oxides is their structure with the general chemical formula AB$_2$O$_4$ (where *A* and *B* are metal ions). Depending on the distribution of ions between the tetrahedral A and octahedral B sites, spinels are divided into three types: normal, inverse, and mixed spinels [8, 9], and the structural formula for a binary spinel may be written in the more accurate format: $\left(A_{1-i}^{p+}B_i^{q+}\right)\left[A_i^{p+}B_{2-i}^{q+}\right]O_4^{2-}$, where the tetrahedral and octahedral sublattices are denoted as () and [], respectively; *p* and *q*—valencies; '*i*'—the inversion parameter, which is 0 for normal, 1 for inverse, and

$0 < i < 1$ for mixed spinels. In addition, the substitution of cations in spinel oxides also significantly affects their physical properties and increases opportunities for their practical application [10–13].

The Mn$_x$Fe$_{3-x}$O$_4$ system has attracted the attention of researchers for a long time [14–16] due to its physical properties depend on the composition, which increases the possible applications of this system [17–22]. At the manganese content $x < 1.9$, it crystallizes in a cubic structure, while at $x > 1.9$ it crystallizes in a tetragonal structure (for bulk and single crystals samples) [23], which originates from the orientation of the tetragonally distorted Mn^{3+}O$_6$ octahedra due to the Jahn–Teller effect [23–25]. Despite the wide variety of compositions of the Mn$_x$Fe$_{3-x}$O$_4$ system, most studies have focused on the iron-rich region (with $x \leq 1$), while the number of reports on the manganese-rich region is limited [26–28]. It has been shown that in the Mn-rich region the system forms in an inverse or a mixed spinel structure [29] and cation distribution can be expressed by two formulae: $\left(Mn^{2+}\right)\left[Fe_{3-x}^{3+}Mn_{x-1}^{3+}\right]O_4^{2-}$ or $\left(Mn_{1-y}^{2+}Fe_y^{3+}\right)\left[Fe_z^{3+}Mn_{2-x}^{3+}Mn_y^{2+}\right]O_4^{2-}$ (where $x = y + z$).

*Correspondence: crlinspin@gmail.com
Department of Applied Physics, National Pingtung University, No. 1
Linsen Rd., Pingtung City 900393, Taiwan

Spivakov *et al. Nanoscale Res Lett*   (2021) 16:162

Page 2 of 7

In the present work, we report, for the first time, as far as we know, about the study of $FeMn_2O_4$ nanoparticles doped with cobalt, which were synthesized by the solvothermal method. The influence of the Co content on the structural and magnetic properties of the nanoparticles was investigated by various methods.

Methods

Synthesis of Co-Doped $FeMn_2O_4$ Nanoparticles

Samples of $Fe(Mn_{1-x}Co_x)_2O_4$ spinel nanoparticles were synthesized by the solvothermal method (Scheme 1). All the reagents were of analytical grade and were used without any further purification. The required quantities of $Fe(acac)_3$, $Mn(acac)_2$ and $Co(acac)_2$ (see Table 1) were dissolved in benzyl alcohol. The resulting solutions were stirred thoroughly and then transferred into a 50 mL Teflon-lined stainless-steel autoclave to a filling capacity of 50%. The crystallization was carried out under autogenous pressure at the temperature of 190 °C for 24 h. Then, the autoclave was cooled naturally to room temperature, and the obtained nanoparticles can be separated from the suspension with a magnetic field. To remove the excess organic solvent and by-products completely, the products were washed several times with ethanol by magnetic decantation and vacuum-dried at room temperature.
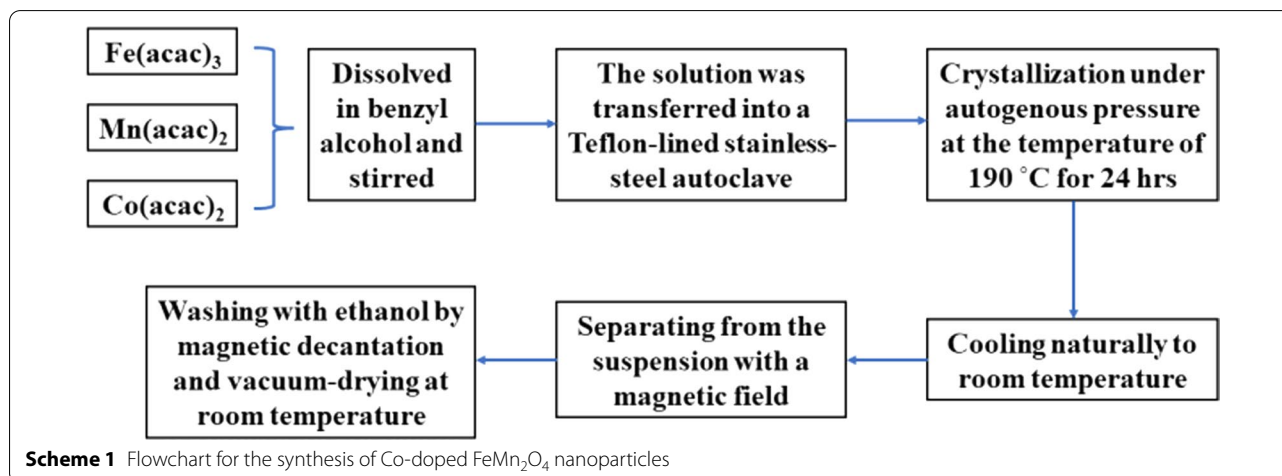
Characterization

The crystal structure and morphology of the nanoparticles were characterized by X-ray diffraction measurements using a Bruker D8 Advance diffractometer (Cu Kα radiation, 40 kV, 25 mA, $\lambda = 1.5418$ Å) and transmission electron microscopy (JEOL JEM-1230 microscope operated at an accelerating voltage of 80 kV). The ICP-MS analysis was carried out using high-resolution ICP-MS system Thermo Scientific ELEMENT XR. The Raman spectra were obtained using a Shamrock 750 spectrograph equipped with a CCD detector. The 533-nm line from the CW He–Ne randomly polarized laser was used for excitation. Magnetic properties were measured by a vibrating sample magnetometer (Lakeshore 7400 series VSM) in the applied field of $H = \pm 17$ kOe.
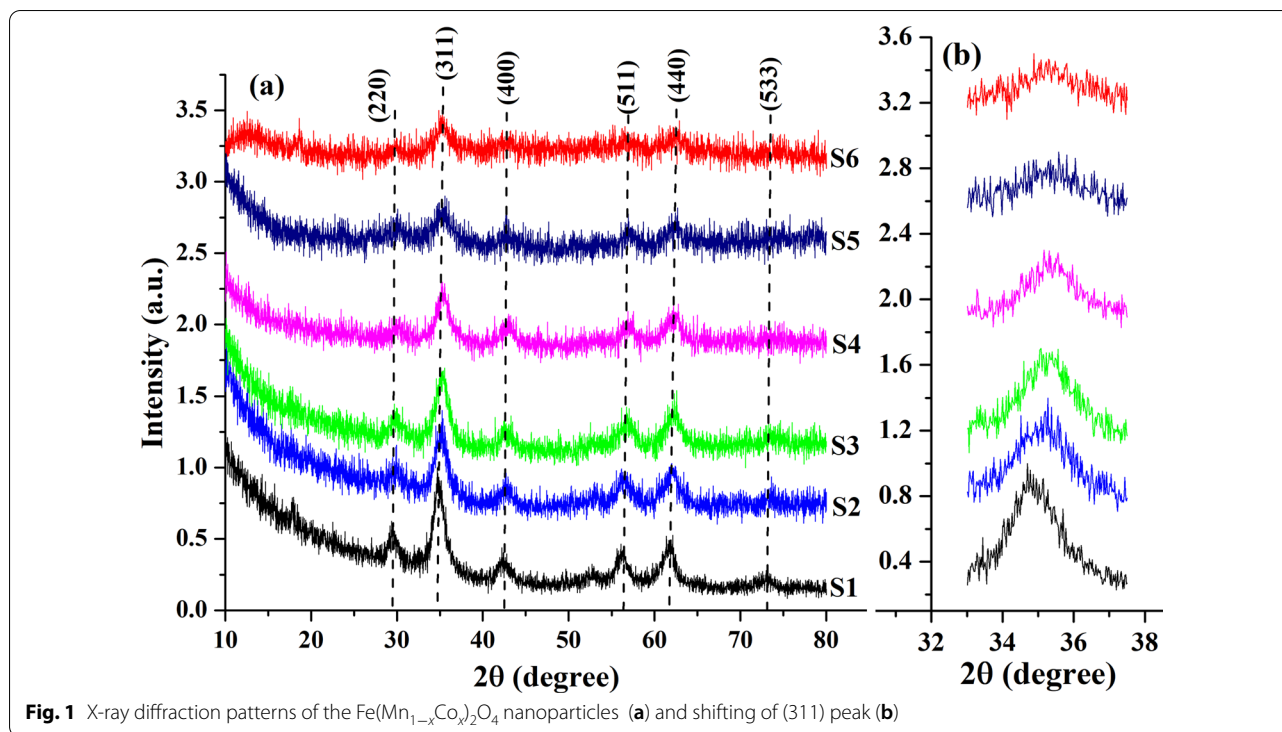
Results and Discussions

The XRD patterns of the samples with various concentrations of cobalt are shown in Fig. 1a. It can be seen that as the Mn content increased, the peaks in XRD spectra become narrower and sharper, which indicates an

Table 1 Composition, abbreviations of the sample names, and quantities of reagents required for the synthesis of the samples

Samples and their abbreviations	Fe(acac)$_3$ (g)	Mn(acac)$_2$ (g)	Co(acac)$_2$ (g)	benzyl alcohol (mL)
$FeMn_2O_4$ (S1)	0.6102	0.8664	0	20
$Fe(Mn_{0.8}Co_{0.2})_2O_4$ (S2)	0.6102	0.6932	0.176	20
$Fe(Mn_{0.6}Co_{0.4})_2O_4$ (S3)	0.6102	0.52	0.3522	20
$Fe(Mn_{0.4}Co_{0.6})_2O_4$ (S4)	0.6102	0.3466	0.5282	20
$Fe(Mn_{0.2}Co_{0.8})_2O_4$ (S5)	0.6102	0.1732	0.7044	20
$FeCo_2O_4$ (S6)	0.6102	0	0.8804	20

Scheme 1 Flowchart for the synthesis of Co-doped $FeMn_2O_4$ nanoparticles

Spivakov *et al. Nanoscale Res Lett*   (2021) 16:162

Page 3 of 7

Fig. 1 X-ray diffraction patterns of the $Fe(Mn_{1-x}Co_x)_2O_4$ nanoparticles (**a**) and shifting of (311) peak (**b**)

increase in the crystallite size of nanoparticles and their better crystallinity. The diffraction peaks at 29.4°, 34.9°, 42.4°, 56.4°, 61.7, and 73.1° correspond to the planes indexed (220), (311), (400), (511), (440), (533), respectively, and they are consistent with standard JCPDS Card No. 10–0319 of jacobsite ferrite with a face-centered cubic structure (space group $Fd\overline{3}m$). Although bulk samples crystallize in a tetragonal structure, a similar XRD patterns indicating the formation of a cubic structure was observed for $FeMn_2O_4$ nanoparticles [17, 18], which may be associated with the existence of a size-dependent phase transition in $FeMn_2O_4$ nanoparticles [30].

The average crystallite size (from the broadening of the most intensive peak (311)) and the lattice parameter of the synthesized samples were calculated in accordance with the relations (1) and (2), and the results are given in Table 1. The calculated values confirmed that crystallite size decreases with the increase in Co content from 9.1 nm (for the sample S1) to 4.4 nm (for the sample S6).

$$d_{XRD} = \frac{0.89\lambda}{\beta\cos\theta}(1); \quad a = d_{hkl}\sqrt{h^2 + k^2 + l^2}(2)$$

where λ—the radiation wavelength (0.15418 nm for Cu Kα); β—the line broadening of a diffraction peak at angle θ; d_{hkl}—inter planar distance; (*hkl*) are the Miller indices.

The results obtained revealed that the lattice parameter ('a') decreases from 8.52 to 8.37 as Co concentration increases. Besides, the data (Fig. 1b) show that

with increasing Co content the position of (311) peak slightly shifts toward higher values of 2θ. This shift as well as the decrease in 'a' are related [31, 32] to the substitution of larger Mn ions ($r_{Mn} = 0.645$ Å) for Co ions ($r_{Co} = 0.545$ Å) on the octahedral sites.

ICP-MS analysis was performed to determine the actual composition of the synthesized samples. The results of the analysis showed that in the range $0 \leq x \leq 0.4$ the actual compositions are in good agreement with expected ones, while in the range $0.4 < x \leq 1$ the actual compositions are slightly shifted toward lower values of *x* (see Table 2), indicating a slight loss of Co during synthesis of these samples.

Table 2 The actual compositions obtained from the results of ICP-MS, the average crystallite sizes calculated by the Scherrer equation (d_{XRD}), and lattice constants (*a*) of the Co-doped $FeMn_2O_4$ nanoparticles

Expected composition	Actual composition	d_{XRD}, nm	*a*, Å
$FeMn_2O_4$	$FeMn_{1.9}O_4$	9.1	8.52
$Fe(Mn_{0.8}Co_{0.2})_2O_4$	$Fe(Mn_{0.8}Co_{0.15})_2O_4$	8.5	8.47
$Fe(Mn_{0.6}Co_{0.4})_2O_4$	$Fe(Mn_{0.6}Co_{0.35})_2O_4$	7.6	8.45
$Fe(Mn_{0.4}Co_{0.6})_2O_4$	$Fe(Mn_{0.35}Co_{0.5})_2O_4$	6.5	8.41
$Fe(Mn_{0.2}Co_{0.8})_2O_4$	$Fe(Mn_{0.2}Co_{0.7})_2O_4$	5.3	8.4
$FeCo_2O_4$	$FeCo_{1.8}O_4$	4.4	8.37

Spivakov *et al. Nanoscale Res Lett*   (2021) 16:162

Page 4 of 7

TEM images for $FeMn_2O_4$ and $FeCo_{1.8}O_4$ samples are shown in Fig. 2 and demonstrate that particles uniform in size and have a spherical or quasi-spherical shape with a tendency to agglomerate. The agglomeration of the nanoparticles may be related to the influence of Van der Waals forces that dominates all other forces when the particle size is less than a few micrometers [33]. Figure 2c and d demonstrates the particle size distribution for the samples S1 and S6 with Gaussian fitting of the distribution. The average particle sizes are 10.5 ± 2 nm ($x=0$) and 5.3 ± 1.5 ($x=0.9$) nm, and these values are in good agreement with the results obtained by XRD.

The Raman spectra of Co-doped $FeMn_2O_4$ nanoparticles in the range of 250–1000 cm^{-1} are presented in Fig. 3. The XRD analysis revealed that the synthesized samples crystallized in a cubic structure and group theoretical analysis for space group $Fd\bar{3}m$ predict [34] five Raman active modes: A_{1g}, E_g, and three T_{2g}. In our samples, only three major peaks were detected in Raman spectra: two intense at ~ 634 cm^{-1} and 479 cm^{-1} one weak at ~ 321 cm^{-1}. Based on the previous studies of Raman spectra of spinel oxides [34, 35], it can be concluded that the Raman peaks correspond to the following modes: peak at ~ 634 cm^{-1} is due to A_{1g} mode involving symmetric stretching of oxygen atoms concerning the metal ions in tetrahedral AO_4 groups. It can also be seen that the peak is broadened for the samples $0 \leq x \leq 0.9$, which is related to the replacement of Mn^{2+} to Co^{2+} ions in tetrahedral sites leading to a redistribution of Mn/Co–O bonds and, as a consequence, broadening of A_{1g} peak. Two low-frequency modes at ~ 321 and ~ 479 cm^{-1} correspond to E_g and $T_{2g}(2)$ modes, respectively, and are related to metal ions involved in octahedral BO_6 sites. The peak at ~ 457 cm^{-1} can be assigned phenyl ring deformation out-of-plane of benzyl alcohol [36], which was used in the synthesis process. Thus, the results of Raman spectroscopy confirmed the cubic structure of the synthesized nanoparticles.
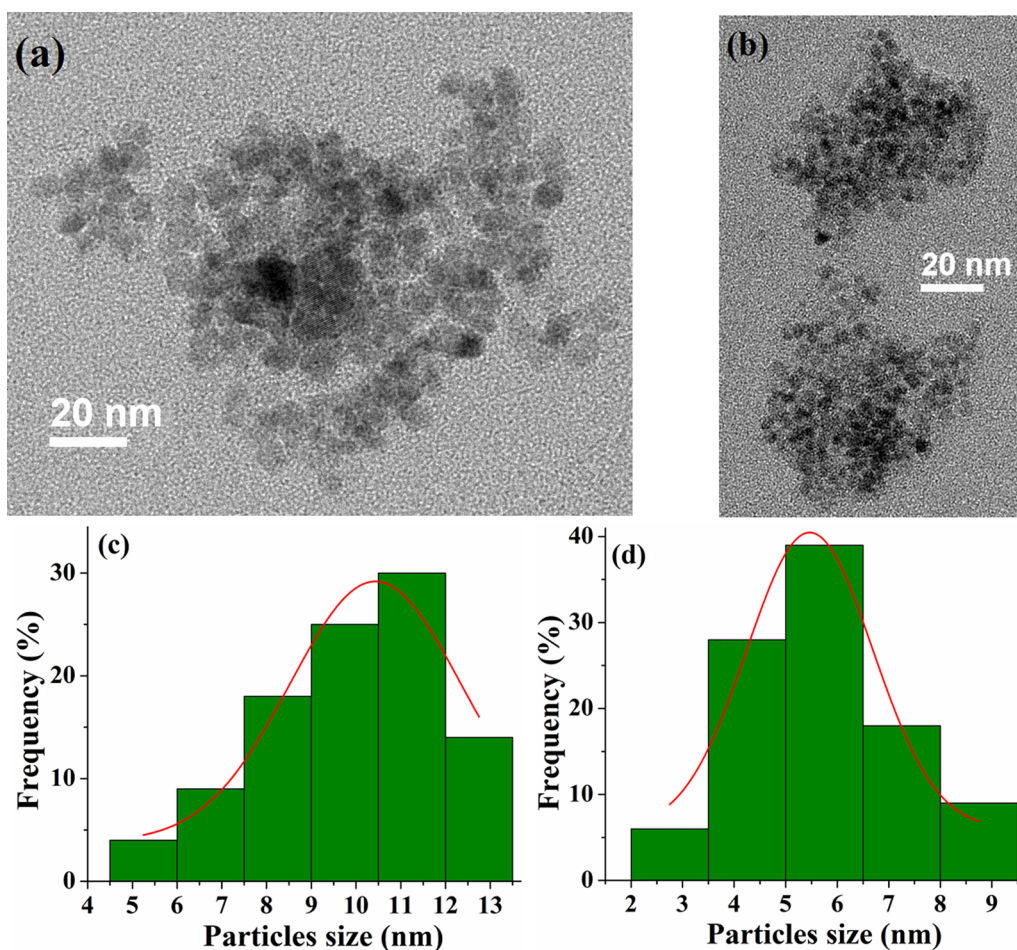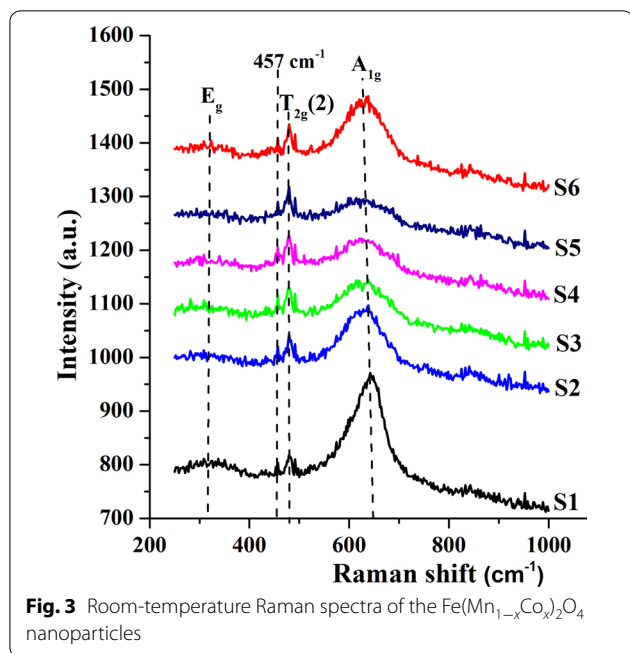

Fig. 2 TEM micrographs of the samples and the histograms of the particle size distribution: (**a**), (**c**) for $FeMn_2O_4$ nanoparticles; (**b**), (**d**) for $FeCo_{1.8}O_4$ nanoparticles

Fig. 3 Room-temperature Raman spectra of the $Fe(Mn_{1-x}Co_x)_2O_4$ nanoparticles
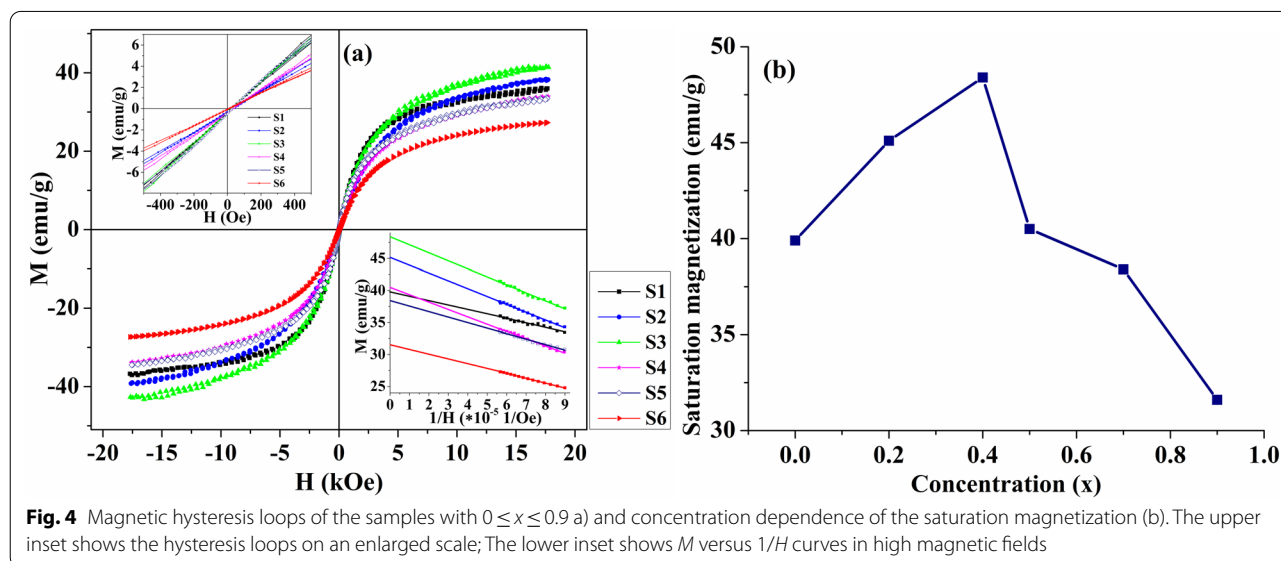
The magnetic hysteresis loops of the $Fe(Mn_{1-x}Co_x)_2O_4$ nanoparticles measured at room temperature are shown in Fig. 4a and b that presents a dependence of the saturation magnetization on cobalt concentration.

As can be seen from Fig. 4a, the magnetic hysteresis loops of the samples are S-like curves with zero remanent magnetization and coercivity, which indicates that all synthesized samples are superparamagnetic at room temperature. The values of the saturation magnetization obtained from the analysis of M versus $1/H$ curves are

presented in Fig. 4b. It should be noted that the value of saturation magnetization for sample S6 is slightly lower than that reported in the literature ($M_S = 40.5$ emu/g) [37] for larger nanoparticles ($d_{XRD} = 21.6$ nm) which can be explained by the influence of the size effect on the magnetic properties. At the same time, the obtained value is higher than for coated $FeCo_2O_4$ nanoparticles ($M_S = 22$ emu/g; $d \sim 40$ nm) [17]. Thus, we can conclude that although the Raman measurements revealed a trace of benzyl alcohol, its presence on the surface of the synthesized nanoparticles is rather small and does not affect their magnetic properties.

The obtained results demonstrate that the saturation magnetization first increases with a corresponding increase in the Co content from 39.9 ($x = 0$) to 48.4 emu/g ($x = 0.4$) and with a further increase in x, the saturation magnetization decreases to 31.6 emu/g ($x = 0.9$). Since an atomic magnetic moment of Co^{2+} (3 μB) is less than magnetic moments of Mn^{2+} and Fe^{3+} (5 μB for both) [38, 39], it is expected the decrease in magnetization with the increase in Co content, which is in agreement with experimental results in the range of $0.4 < x \leq 0.9$. However, for the concentration range $0 \leq x \leq 0.4$, an increase in the saturation magnetization is observed with increasing x, which can be explained by the redistribution of cations between tetrahedral and octahedral sites. In accordance with Néel's two-sublattice theory, inter-sublattice interaction (A—B) is much stronger than the intra-sublattice interactions (A—A and B—B) and the net magnetization is proportional to the difference between the magnetic moment of tetrahedral (M_A) and octahedral (M_B) sites and is given by $M_S = M_B - M_A$ [40]. It is assumed that at low

Fig. 4 Magnetic hysteresis loops of the samples with $0 \leq x \leq 0.9$ a) and concentration dependence of the saturation magnetization (b). The upper inset shows the hysteresis loops on an enlarged scale; The lower inset shows M versus $1/H$ curves in high magnetic fields

Spivakov *et al. Nanoscale Res Lett*   (2021) 16:162

Page 6 of 7

concentration Co^{2+} ions push Fe^{3+} ions from tetrahedral to octahedral B sites, which leads to an increase in the octahedral magnetic moment due to an increase in Fe^{3+} ions and, as a result, an increase in the net magnetization.

Conclusions

The effect of Co doping on the structural and magnetic properties of $Fe(Mn_{1-x}Co_x)_2O_4$ nanoparticles prepared by the solvothermal method was studied. The results of the structural analysis showed that particles are uniform in size and have spherical or quasi-spherical shapes, herewith with the increase in cobalt content, the average particle size decreases from 10.5 ± 2 nm ($x = 0$) to 5.3 ± 1.5 ($x = 0.9$) nm. Although bulk and single crystal samples of $FeMn_2O_4$ crystallize in a tetragonal structure, the results of XRD and Raman showed that the synthesized nanoparticles crystallized in a cubic structure, which may indicate the existence of a size-dependent phase transition in $FeMn_2O_4$. Magnetic measurements revealed the superparamagnetic nature of all samples at room temperature. It has been found that in the range of $0.4 < x \leq 0.9$ the saturation magnetization decreases, as expected. However, for the range of $0 \leq x \leq 0.4$, an increase in the saturation magnetization is observed. Such behavior can be associated with the redistribution of Fe^{3+} ions between tetrahedral and octahedral sites.

Declarations

References

1. Hirohata A, Takanashi K (2014) Future perspectives for spintronic devices. J Phys D Appl Phys 47:193001. https://doi.org/10.1088/0022-3727/47/19/193001
2. Wu L, Mendoza-Garcia A, Li Q, Sun S (2016) Organic phase syntheses of magnetic nanoparticles and their applications. Chem Rev 116:10473–10512. https://doi.org/10.1021/acs.chemrev.5b00687
3. Padmanathan N, Selladurai S (2014) Mesoporous MnCo2O4 spinel oxide nanostructure synthesized by solvothermal technique for supercapacitor. Ionics 20:479–487. https://doi.org/10.1007/s11581-013-1009-8
4. Amiri M, Salavati-Niasari M, Akbari A (2019) Magnetic nanocarriers: evolution of spinel ferrites for medical applications. Adv Colloid Interface Sci 265:29–44. https://doi.org/10.1016/j.cis.2019.01.003
5. Goldstein A, Shames AI, Stevenson AJ, Cohen Z, Vulfson M (2013) Parasitic Light absorption processes in transparent polycrystalline MgAl2O4 and YAG. J Am Ceram Soc 96:3523–3529. https://doi.org/10.1111/jace.12525
6. Kirankumar VS, Sumathi S (2020) A review on photodegradation of organic pollutants using spinel oxide. Mater Today Chem 18:100355. https://doi.org/10.1016/j.mtchem.2020.100355
7. Belous A, Tovstolytkin A, Solopan S, Shlapa Yu, Fedorchuk O (2018) Synthesis, properties and applications of some magnetic oxide based nanoparticles and films. Acta Phys Pol A 133:1006–1012. https://doi.org/10.12693/APhysPolA.133.1006
8. Verwey EJW, Heilmann EL (1947) Physical properties and cation arrangements of oxides with spinel structures. I. Cation arrangements in spinels. J Chem Phys 15:174–80. https://doi.org/10.1063/1.1746464
9. O'Neill HSC, Navrotsky A (1983) Simple spinels; crystallographic parameters, cation radii, lattice energies, and cation distribution. Am Miner 68:181–194
10. Paudel TR, Zakutayev A, Lany S, d'Avezac M, Zunger A (2011) Doping rules and doping prototypes in A2BO4 spinel oxides. Adv Funct Mater 21:4493–4501. https://doi.org/10.1002/adfm.201101469
11. Dwivedi S, Sharma R, Sharma Y (2014) Electroconductive properties in doped spinel oxides. Optic Mater 37:656–665. https://doi.org/10.1016/j.optmat.2014.08.010
12. Deepak FL, Bañobre-Lopez M, Carbo-Argibay E, Cerqueira MF, Piñeiro-Redondo Y, Rivas J, Thompson CM, Kamali S, Rodriguez-Abreu C, Kovnir K, Kolenko YV (2015) A systematic study of the structural and magnetic properties of Mn-, Co-, and Ni-doped colloidal magnetite nanoparticles. J Phys Chem C 119:11947–11957. https://doi.org/10.1021/acs.jpcc.5b01575
13. Kolhatkar AG, Jamison AC, Litvinov D, Willson RC, Lee TR (2013) Tuning the magnetic properties of nanoparticles. Int J Mol Sci 14:15977–16009. https://doi.org/10.3390/ijms140815977
14. Penoyer RF, Shafer MW (1959) On the magnetic anisotropy in manganese-iron spinels. J Appl Phys 30:315S-316S. https://doi.org/10.1063/1.2185951
15. Crapo WA (1960) Time decrease of initial permeability in $Mn_xFe_{3-x}O_{4+y}$. J Appl Phys 31:267S-268S. https://doi.org/10.1063/1.1984692
16. Tanaka M, Mizoguchi T, Aiyama Y (1963) Mössbauer effect in $Mn_xFe_{3-x}O_4$. J Phys Soc Jpn 18:1091. https://doi.org/10.1143/JPSJ.18.1091
17. Amoli-Diva M, Asli MD, Karimi S (2017) FeMn2O4 nanoparticles coated dual responsive temperature and pH-responsive polymer as a magnetic nano-carrier for controlled delivery of letrozole anti-cancer. Nanomed J 4:218–223. https://doi.org/10.22038/NMJ.2017.04.003
18. Nagamuthu S, Vijayakumar S, Lee S-H, Ryu K-S (2016) Hybrid supercapacitor devices based on MnCo2O4 as the positive electrode and FeMn2O4 as the negative electrode. Appl Surf Sci 390:202–208. https://doi.org/10.1016/j.apsusc.2016.08.072
19. Liu Y, Zhang N, Yu C, Jiao L, Chen J (2016) MnFe2O4@C nanofibers as high-performance anode for sodium-ion batteries. Nano Lett 16:3321. https://doi.org/10.1021/acs.nanolett.6b00942
20. Yamaguchi NU, Bergamasco R, Hamoudi S (2016) Magnetic MnFe2O4—graphene hybrid composite for efficient removal of glyphosate from water. Chem Eng J 295:391–402. https://doi.org/10.1016/j.cej.2016.03.051

Spivakov *et al. Nanoscale Res Lett*   (2021) 16:162

Page 7 of 7

21. Vignesh RH, Sankar KV, Amaresh S, Lee YS, Selvan RK (2015) Synthesis and characterization of $MnFe_2O_4$ nanoparticles for impedometric ammonia gas sensor. Sens Actuators B 220:50–58. https://doi.org/10.1016/j.snb.2015.04.115

22. Kim J, Cho HR, Jeon H, Kim D, Song C, Lee N, Choi SH, Hyeon T (2017) Continuous O_2 evolving $MnFe_2O_4$ nanoparticle-anchored mesoporous silica nanoparticles for efficient photodynamic therapy in hypoxic cancer. J Am Chem Soc 139:10992–10995. https://doi.org/10.1021/jacs.7b05559

23. Brabers VAM (1969) Infrared spectra of cubic and tetragonal manganese ferrites. Phys Stat Solid 33:563. https://doi.org/10.1002/pssb.19690330209

24. Kanamori J (1960) Crystal distortion in magnetic compounds. J Appl Phys 31:14S-23S. https://doi.org/10.1063/1.1984590

25. Dunitz JD, Orgel LE (1957) Electronic properties of transition-metal oxides—I: distortions from cubic symmetry. J Phys Chem Sol 3:20–29. https://doi.org/10.1016/0022-3697(57)90043-4

26. Nepal R, Zhang Q, Dai S, Tian W, Nagler SE, Jin R (2018) Structural and magnetic transitions in spinel $FeMn_2O_4$ single crystals. Phys Rev B 97:024410. https://doi.org/10.1103/PhysRevB.97.024410

27. Naito K, Inaba H, Yagi H (1981) Heat capacity measurements of $Mn_xFe_{3-x}O_4$. J Sol Sta Chem 36:28–35. https://doi.org/10.1016/0022-4596(81)90188-2

28. Lahiri P, Sengupta SK (1995) Physico-chemical properties and catalytic activities of the spinel series $Mn_xFe_{3-x}O_4$ towards peroxide decomposition. J Chem Soc Faraday Trans 91:3489–3494. https://doi.org/10.1039/FT9959103489

29. Gillot B, Laarj M, Kacim S (1997) Reactivity towards oxygen and cation distribution of manganese iron spinel $Mn_{3-x}Fe_xO_4$ ($0 \leq x \leq 3$) fine powders studied by thermogravimetry and IR spectroscopy. J Mater Chem 7:827–831. https://doi.org/10.1039/A607179A

30. Liu L, Zhao R, Xiao C, Zhang F, Pevere F, Shi K, Huang H, Zhong H, Sychugov I (2019) Size-dependent phase transition in perovskite nanocrystals. J Phys Chem Lett 10:5451–5457. https://doi.org/10.1021/acs.jpclett.9b02058

31. Li C, Han X, Cheng F, Hu Y, Chen C, Chen J (2015) Phase and composition controllable synthesis of cobalt manganese spinel nanoparticles towards efficient oxygen electrocatalysis. Nat Commun 6:7345. https://doi.org/10.1038/ncomms8345

32. Yousuf MA, Baig MM, Waseem M, Haider S, Shakir I, Khan SU-D, Warsi MF (2019) Low cost micro-emulsion route synthesis of Cr-substituted $MnFe_2O_4$ nanoparticles. Ceram Int 45:22316–22323. https://doi.org/10.1016/j.ceramint.2019.07.259

33. Werth JH, Linsenbuhler M, Dammer SM, Farkas Z, Hinrichsen H, Wirth K-E, Wolf DE (2003) Agglomeration of charged nanopowders in suspensions. Powder Technol 133:106–112. https://doi.org/10.1016/S0032-5910(03)00096-2

34. White WB, De Angelis BA (1967) Interpretation of the vibrational spectra of spinels. Spectrochem Acta 23A:985–995. https://doi.org/10.1016/0584-8539(67)80023-0

35. Graves PR, Johnston C, Campaniello JJ (1988) Raman scattering in spinel structure ferrites. Mater Res Bull 23:1651–1660. https://doi.org/10.1016/0025-5408(88)90255-3

36. Prystupa DA, Anderson A, Torrie BH (1994) Raman and infrared study of solid benzyl alcohol. J Raman Spectrosc 25:175–182. https://doi.org/10.1002/jrs.1250250206

37. Zhou R, Zhao J, Shen N, Ma T, Su Y, Ren H (2018) Efficient degradation of 2,4-dichlorophenol in aqueous solution by peroxymonosulfate activated with magnetic spinel $FeCo_2O_4$ nanoparticles. Chemosphere 197:670–679. https://doi.org/10.1016/j.chemosphere.2018.01.079

38. Concas G, Spano G, Cannas C, Musinu D, Peddis GP (2009) Inversion degree and saturation magnetization of different nanocrystalline cobalt ferrites. J Magn Magn Mater 321:1893–1897. https://doi.org/10.1016/j.jmmm.2008.12.001

39. Ghodake UR, Chaudhari ND, Kambale RC, Patil JY, Suryavanshi SS (2016) Effect of Mn^{2+} substitution on structural, magnetic, electric and dielectric properties of Mg–Zn ferrites. J Magn Magn Mater 407:60–68. https://doi.org/10.1016/j.jmmm.2016.01.022

40. Thakur SS, Pathania A, Thakur P, Thakur A, Hsu J-H (2015) Improved structural, electrical and magnetic properties of Mn–Zn–Cd nanoferrites. Ceram Int 41:5072–5078. https://doi.org/10.1016/j.ceramint.2014.12.077

Publisher's Note